coatings

MDPI

Article

Spectral Characteristics of Biomimetic Micro-Nano Structures Derived from Saharan Silver Ants—A Simulation Study

Mingyue Liu [1], Bo Chen [2,3,*], Dehai Zhang [1] and Jian Chen [3,4]

[1] Key Laboratory of Microwave Remote Sensing, National Space Science Center, Chinese Academy of Sciences, Beijing 100190, China
[2] College of Materials Science and Opto-Electronic Technology, Chinese Academy of Sciences, Beijing 100049, China
[3] Aerospace Information Research Institute, Chinese Academy of Sciences, Beijing 100190, China
[4] School of Electronic, Electrical and Communication Engineering, Chinese Academy of Sciences, Beijing 100049, China
* Correspondence: cbo_111@163.com

Abstract: Proper selections of microwave-transmitting thermal control materials play key roles in the orbit operations of aerospace microwave detectors. Currently, white paint and germanium-coated polyimide film are common choices for microwave-transmitting thermal control, which have been extensively studied from the perspective of material compositions, ignoring the influence of the micro-nano structure on the surface of the material. Inspired by Saharan silver ants relying on micro-nano structures of hairs for heat protection and dissipation, in this paper, based on finite element simulation, spectral characteristics (e.g., solar absorptance and infrared emissivity) of three types of biomimetic micro-nano structures (e.g., including pyramid, tetrahedron, and triangular prism) were studied and compared. Simulation results revealed that spectral characteristics of these biomimetic micro-nano structures were mainly regulated by the tip height and the air gap; the decrease of the tip height led to the decrease in the solar absorptance and the infrared emissivity; the solar absorptance was decreased, and the infrared emissivity was increased with the increase of the air gap. When these biomimetic structures were compared with flat surfaces without micro-nano topographies, a decrease of the solar absorptance to block the incidence of heat flow from the sun and an increase of the infrared emissivity to dissipate its own heat to the space were located, which may give suggestions on the adjustment of spectral characteristics of aerospace microwave-transmitting thermal control materials.

Keywords: spectral characteristics; micro-nano structure; solar absorptance; infrared emissivity; biomimetic silver ant

check for updates

Citation: Liu, M.; Chen, B.; Zhang, D.; Chen, J. Spectral Characteristics of Biomimetic Micro-Nano Structures Derived from Saharan Silver Ants—A Simulation Study. *Coatings* **2023**, *13*, 85. https://doi.org/10.3390/coatings13010085

Academic Editor: Rafael L. Quirino

Received: 12 November 2022
Revised: 26 December 2022
Accepted: 31 December 2022
Published: 3 January 2023

Copyright: © 2023 by the authors. Licensee MDPI, Basel, Switzerland. This article is an open access article distributed under the terms and conditions of the Creative Commons Attribution (CC BY) license (https://creativecommons.org/licenses/by/4.0/).

1. Introduction

It is highly necessary to integrate proper microwave-transmitting thermal control materials into aerospace microwave detectors to create an environment with certain temperature variations. At present, the commonly used microwave-transmitting thermal control materials for aerospace microwave detectors include thermal control coatings and germanium-coated polyimide film. Among them, coating materials of thermal control, such as white paint [1], are not compatible with microwave antennas based on microelectronic arrays. Moreover, exposed to long-term radiation in space environments, the optical and electrical properties of white paint were shown to degrade [2,3], leading to compromised performances of thermal control. Meanwhile, the germanium-coated polyimide film [4–6] was shown to successfully cover the surfaces of the microwave antennas based on microfabrication. However, germanium is unstable in ground storage and/or transportation and would rapidly degrade. Even in the environment of clean storage with strictly sealed packaging, its storage time was still very short [6,7].

Currently, the studies of improving the temporal and spatial stability of these materials have mainly focused on the composition optimization of the corresponding materials [6–8]. The influences of micro-nano structures on the surface of materials were ignored, which led to certain limitations.

There are some structures in nature that demonstrate unique thermal control characteristics, such as penguins [9], polar bears [10] and Saharan silver ants [11]. Among them, in 1992, Wehenr et al. [12] discovered that Saharan silver ants maintained body temperature within 53.6 °C under the environmental surface temperature as high as 70 °C. In 2015, Shi et al. [11] found that micro-nano structures of silver ant hair played key roles in heat protection and dissipation, while the triangular cross section of the hair and the air gap were the most critical factors. The study compared the reflective properties of triangular and circular hairs of the same central cross-sectional area, and the simulation results showed that the reflectivity of triangular hairs was higher than circular hairs in the visible band. This study could have a significant technological impact by inspiring the development of biomimetic micro-nano structures. The material of hairs of silver ants is the chitin-protein complex, which is microwave-transmitted.

In 2017, inspired by the thermoregulatory mechanisms of Saharan silver ants, Zhai et al. [13] made the randomized glass-polymer hybrid metamaterial. This implied the great potential for biomimetic micro-nano structures derived from Saharan silver ants. It limited the transmission of microwave radiation because the silver coating was used to reflect solar irradiation, and it would reflect microwaves. However, Saharan silver ants relied on micro-nano structures of the hair for the reflection of the solar, which avoided the use of metallic materials. In 2020, Wu et al. [14] fabricated flexible passive radiative cooling by mimicking the hairs of Saharan silver ants. In more detail, the pyramidal structures on polydimethylsiloxane (PDMS) mimicked the triangular cross section of the hair and the air gap. The microwave could penetrate PDMS, but PDMS was not suitable for aerospace engineering. Besides, no further studies explored the influence of the heights of the tip and the air gap or other similar structures (e.g., tetrahedron and triangular prism).

In this paper, the thermal control properties of Saharan silver ants were introduced into the study of microwave-transmitting thermal control materials of aerospace microwave detectors. Inspired by Saharan silver ants relying on micro-nano structures of hairs for heat protection and dissipation, based on finite element simulation, spectral characteristics (e.g., solar absorptance and infrared emissivity) of three types of biomimetic micro-nano structures (e.g., including pyramid, tetrahedron and triangular prism) were studied and compared. In addition, the relationships between spectral characteristics and geometrical dimensions (e.g., the tip height and the air gap) of biomimetic structures were studied. This article may provide some references for the adjustment of spectral characteristics of aerospace microwave-transmitting thermal control materials and new ideas for the regulation of thermal control characteristics of aerospace microwave detectors.

2. Materials and Methods

Polyimide was selected as the material of these biomimetic micro-nano structures, which is a microwave-transmitted, non-metallic material and widely used in satellites such as multilayer insulation materials and germanium-coated polyimide films.

The governing equation can be written in the form of a wave equation [15] as follows:

$$\nabla \times \left(\mu_r^{-1} \nabla \times \boldsymbol{E}\right) - k_0^2 \varepsilon_r \boldsymbol{E} = 0 \quad (1)$$

where $\boldsymbol{E}$ is the electric field intensity, k_0 is the wave number of free space, $k_0 = 2\pi/\lambda_0$, λ_0 is the wavelength of free space, μ_r is the relative permeability of the material, ε_r is the relative permittivity of the material, n is the refractive index. When $\mu_r = 1$, $\varepsilon_r = n^2$. The equation can alternatively be written as:

$$\nabla \times (\nabla \times \boldsymbol{E}) - \left(\frac{2\pi}{\lambda_0}\right)^2 n^2 \boldsymbol{E} = 0 \quad (2)$$

When the equation is written using the refractive index, the assumption is that the relative permeability $\mu_r = 1$ and the electrical conductivity $\sigma = 0$ and only the constitutive relations for linear materials are available.

The reflectivity was obtained by resolving Equation (3) [15] as follows:

$$R = \left| \frac{\int_{port1} (\boldsymbol{E}_{11} - \boldsymbol{E}_{10}) \cdot \boldsymbol{E}_{10} dA}{\int_{port1} \boldsymbol{E}_{10} \cdot \boldsymbol{E}_{10} dA} \right|^2 \quad (3)$$

where R is the reflectivity, port 1 is the excitation port, dA is the area element of port 1, $\boldsymbol{E_{10}}$ is the excitation electric field intensity on port 1, $\boldsymbol{E_{10}} = [0, E_{10y}, 0]$, $\boldsymbol{E_{11}}$ is the computed electric field intensity on the port 1.

$$E_{10y} = \sqrt{\frac{2P_{in}/A}{c_0 n \varepsilon_0}} \quad (4)$$

where E_{10y} is the projection of $\boldsymbol{E_{10}}$ in the y direction, P_{in} is the power of the transverse electric (TE) wave excitation at port 1, P_{in} = 1W, A is the area of port 1, c_0 is the speed of light in vacuum, c_0 = 299,792,458 m/s, n is the refractive index, ε_0 is the vacuum permittivity, $\varepsilon_0 = 8.854187817 \times 10^{-12}$ F/m.

As shown in Figure 1a,b [11], the hair structure of silver ants gradually tapers off toward the tip with a triangular cross section and a characteristic size at the micro/nanoscale. The hair of sliver ants displays unique spectral characteristics which originate from its peculiar micro-nano structures, specifically enhancing the reflectivity in the visible and near-infrared ranges and the emissivity in the mid-infrared range of the spectrum.

Based on the micro-nano structures of the hair of silver ants, numerical simulations of the biomimetic micro-nano structures were conducted to determine the effects of structural parameters on spectral characteristics. Three types of biomimetic micro-nano structures made of pyramid, tetrahedron, and triangular prism are shown in Figure 1c.

For arrayed biomimetic micro-nano structures with individual units, feature sizes mainly include tip height h_1 to model the triangular hairs of silver ants, tip width d_1, film height h_2 to model the triangular hairs of silver ants, period length d_2, air gap h_3 to model the air gap of silver ants, body height h_4 to model the body of silver ants (see Figure 1d). Based on the structural parameters of silver ants, the default parameters were set as h_1 = 200 nm, d_1 = 200 nm, h_2 = 200 nm, d_2 = 250 nm, h_3 = 150 nm and h_4 = 200 nm.

In order to investigate the effects of the tip height h_1 and air gap h_3 on the spectral characteristics of the biomimetic micro-nano structure, h_1 was set as 50 nm, 100 nm, 200 nm, 400 nm and 600 nm, and h_3 as 50 nm, 150 nm, 300 nm and 500 nm. The materials for the tip, film and body of the biomimetic micro-nano structures were polyimide with n_{PI} = 1.55 and air with n_{air} = 1 for the air gap.

After the geometric modeling of the biomimetic micro-nano structures, the grid was divided, as shown in Figure 1e, based on tetrahedral elements with three-dimensional electromagnetic vector field degrees of freedom. Then, the visible, near-infrared and mid-infrared ranges of the spectrum (0.39~25 μm) were used as incident loads. Surfaces in the directions perpendicular to the x-axis and y-axis were set as floquet periodic boundary conditions. The spectral reflectance curves were obtained using the finite element method based on the frequency domain, where the corresponding development of solar absorptance and infrared emissivity could be observed.

In order to validate the simulation method, the spectral reflectance curve obtained by simulation in [11] was reproduced using the above method. The two-dimensional and three-dimensional simulation structures were shown in Figure S1a,b, respectively, including (I) air, (II) triangular hair, (III) air gap and (IV) body. The feature sizes were 2.5 μm, 2 μm, 0.6 μm and 2 μm, respectively. The other parameters and the approach to obtaining the spectral reflectance curves were the same as described above.

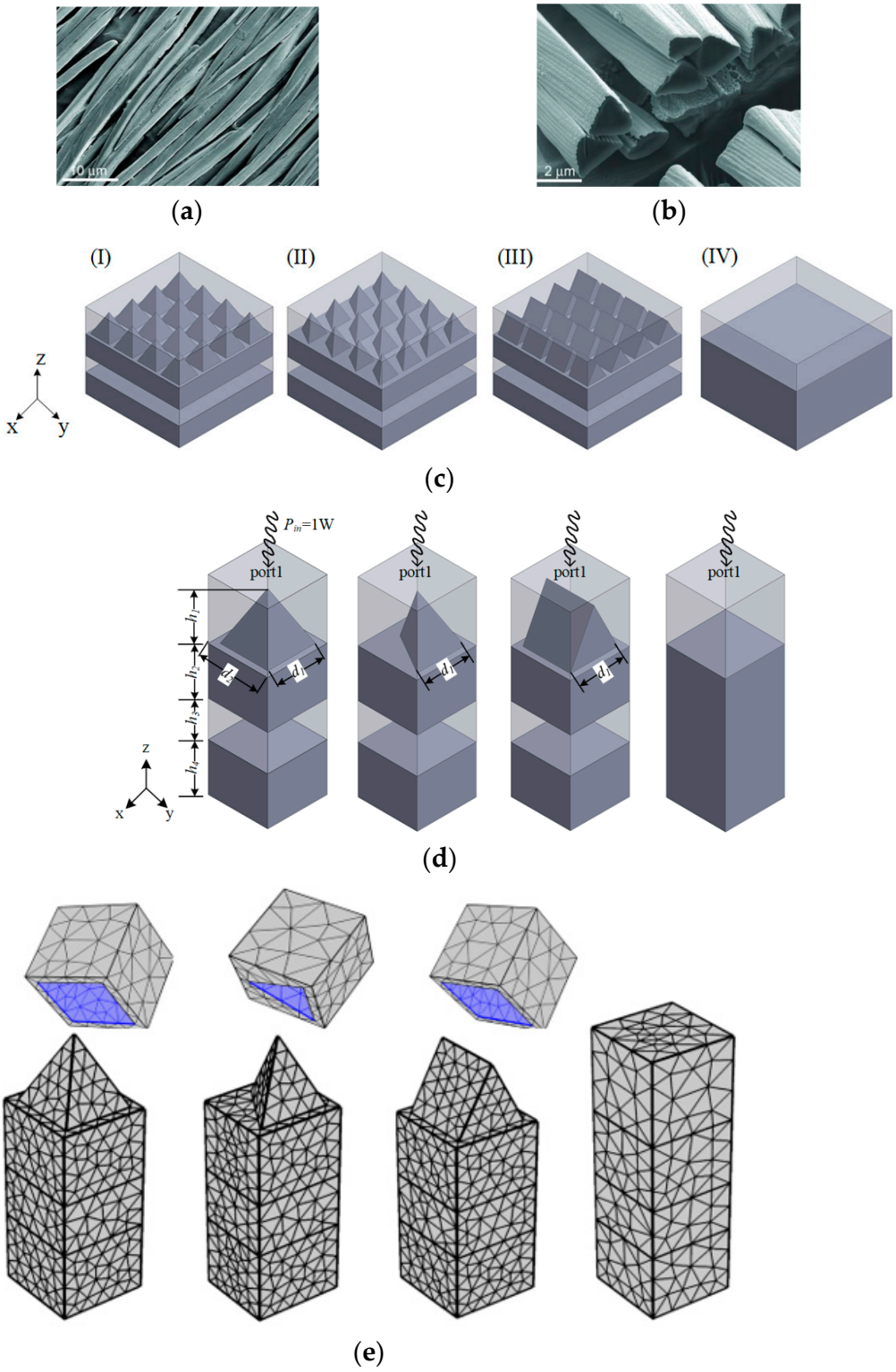


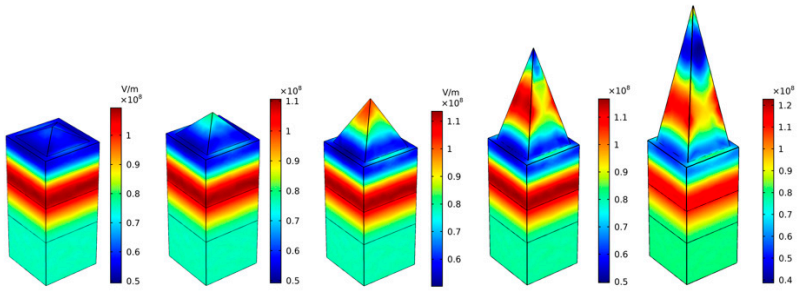
Figure 1. Hairs of Saharan silver ants and their biomimetic counterparts at the micro-nano scale. (**a**) Axial and (**b**) central cross-sectional images of SEM to illustrate the hairs of the real Saharan silver ants [11]. (**c**) Arrayed biomimetic micro-nano structures with individual units (e.g., pyramid (I), tetrahedron (II), triangular prism (III) and flat surface (IV) for comparison) before (**d**) and after (**e**) meshing with finite elements.

3. Results and Discussion

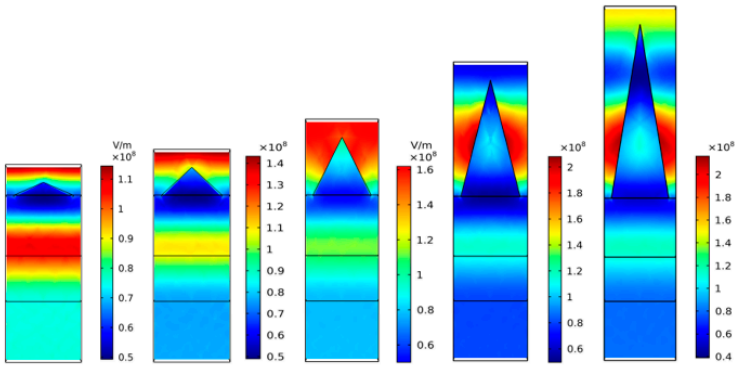
Figure S2 shows the distributions of the electric field intensities obtained by the simulation of literature [11] (a) and this study (b) under the incident wavelengths of 0.652 µm, 0.909 µm, 1.333 µm, 1.704 µm, and 2.880 µm, respectively. In this study, the electric field intensity distribution of the two-dimensional model and the central cross section of the three-dimensional model were identical. Therefore, Figure S2b represents the electric field intensity distribution of the two-dimensional and the central cross section of the three-dimensional model at the same time. As shown in Figure S2a,b, the distributions of the electric field intensities obtained by the simulation of literature [11] and this study were basically consistent, and the consistency was higher at higher wavelengths, validating the simulation method developed in this paper.

Figure S2c,d show the spectral reflectance curves obtained from the literature [11] and this study, respectively. In this study, the spectral reflectance curves of the 2D model and the 3D model were identical; therefore, Figure S2d represented the spectral reflectance curves of both the 2D model and the 3D model. As shown in Figure S2c,d, when the incident wavelengths were 0.652 µm, 0.909 µm, 1.333 µm, 1.704 µm, and 2.880 µm, the peak positions of the two curves obtained from the literature [11] and this study were consistent, and the peak height tended to be more consistent with the increase of wavelength, which further verified the simulation method in this paper.

Figure 2a–d show images of three-dimensional and central cross-sectional distributions of the electrical field intensities for the pyramidal micro-nano structures with a variety of tip heights (50, 100, 200, 400 and 600 nm) under the wavelength of 0.99 µm (a and b) and 9.99 µm (c and d), respectively. As the tip height was decreased, the electric field intensity at the incident port was shown to increase at 0.99 µm. The closer the color of the area near the excitation port 1 was to red, the greater the electric field intensity, the higher portion of the incident light reflected back, and the larger the reflectivity of the structure. As to the electric field intensity at 9.99 µm, no significant changes were found.



(**a**)



(**b**)

Figure 2. *Cont.*

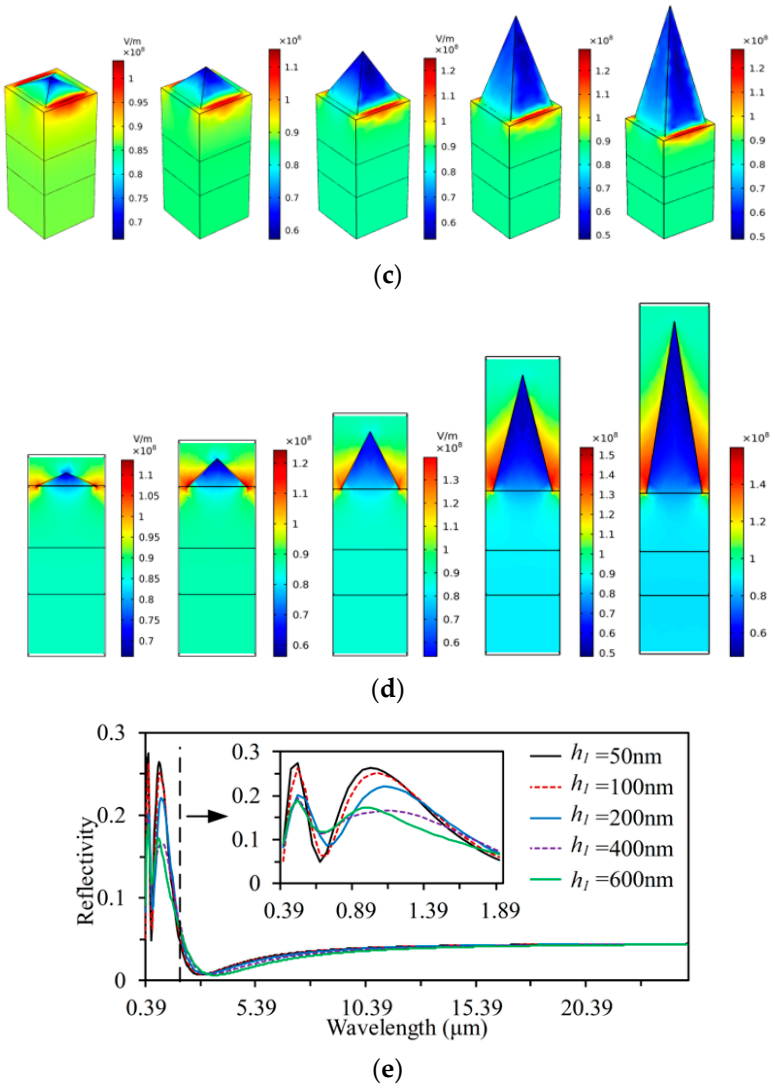


Figure 2. Numerical results of spectral characteristics of pyramidal biomimetic micro-nano structures as a function of tip height. Images of three-dimensional and central cross-sectional distributions of the electrical field intensity for the pyramidal micro-nano structures with a variety of tip heights (50, 100, 200, 400 and 600 nm) under the wavelength of 0.99 μm (**a**,**b**) and 9.99 μm (**c**,**d**), respectively. (**e**) Spectral reflectance curves of pyramidal biomimetic micro-nano structures modulated by tip height indicate that a decrease in tip height can decrease the solar absorptance and the infrared emissivity.

Figure 2e shows spectral reflectance curves of pyramidal biomimetic micro-nano structures modulated by tip height. As the tip height was decreased, the maximum reflectivity in visible and near-infrared ranges of the spectrum (0.39~2.5 μm) increased, while the reflectivity in the mid-infrared range of the spectrum (2.5~25 μm) was also increased, revealing that as the height of the micro-nano structure decreased, the solar absorptance and the infrared emissivity decreased.

In order to obtain the optimized geometric parameters for a final design, Tian et al. [16] investigated the geometric effects on the proposed grating-Mie-metamaterial based solar absorbers. The thickness of the top grating layer of the 2-D triangular surface gratings was studied. As the thickness of the top grating layer was decreased, the reflectivity over visible and near-infrared regimes increased, which followed similar rules to this paper. An ideal solar absorber should increase the solar absorptance over the visible and near-infrared regimes to convert most radiations into heat. However, in this paper, thermal control materials of aerospace microwave detectors should decrease the solar absorptance to block the incidence of heat flows from the sun.

According to Fresnel's law, reflectance is related to the refractive index of both media. The closer the refractive index of two media is, the lower the reflectance is.

According to the effective medium theory, the tip of the pyramidal micro-nano structure was divided into n parts, the thickness of each part was Δh, Δh = 5 nm, and z represented the height of each part. Figure 3 represented the central cross section of the tip of the pyramidal micro-nano structure. The tip of the pyramidal micro-nano structure was located in a cube whose width was equal to the array period d_2 of the pyramidal micro-nano structure. z = 0 represented the bottom of the tip, and its width d_1 was 200 nm. The height of the tip h_1 decreased from 600 nm to 50 nm, and the width of each layer was $d(z)$, as follows:

$$d(z) = \frac{h_1 - z}{h_1} d_1 \tag{5}$$

where z was the height of each part, d_1 was the width of the tip, h_1 was the height of the tip, and $d(z)$ was the width of each layer.

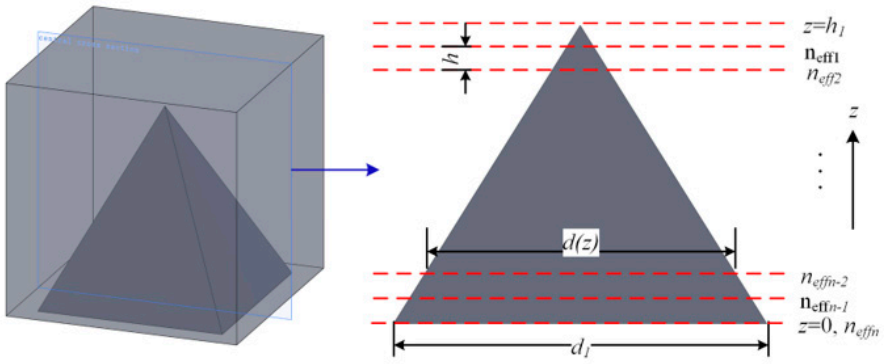


Figure 3. Effective multi-layer model of the tip of the pyramidal micro-nano structure.

The filling rate f_j of each layer could be obtained as follows:

$$d(z) = \frac{h_1 - z}{h_1} d_1 \tag{6}$$

where d_2 was the width of the cube, $d(z)$ was the width of each layer, and f_j was the filling rate of the jth layer of the tip.

The variation of the effective permittivity ε varied with the filling rate f_j. When the excitation at port 1 was the TE wave, the zeroth-order approximation of the effective permittivity [17] was represented by:

$$\varepsilon_{jTE}^{(0)} = f_j \varepsilon_{PI} + (1 - f_j)\varepsilon_{air} \tag{7}$$

where $\varepsilon_{jTE}{}^{(0)}$ was the zeroth-order approximation of the effective permittivity (jth layer of the tip) for the TE wave, f_j was the filling rate of the jth layer of the tip, ε_{PI} was the permittivity of polyimide, ε_{air} was the permittivity of air.

This estimation was accurate only when the profile period of the micro-nano structure was much smaller than the incident wavelength. When the wavelength was only a few times larger than the structure (e.g., sunlight interacting with the biomimetic micro-nano structure), the use of second-order approximation became necessary.

$$\begin{aligned} \varepsilon_{jTE}^{(2)} &= \varepsilon_{jTE}^{(0)} \left[1 + \frac{\Delta \varepsilon_j}{\beta^2} \right] \\ &= \varepsilon_{jTE}^{(0)} \left[1 + \frac{\pi^2}{3} \left(\frac{d_2}{\lambda} \right)^2 f_j^2 (1 - f_j)^2 \frac{(\varepsilon_{PI} - \varepsilon_{air})^2}{\varepsilon_0 \varepsilon_{jTE}^{(0)}} \right] \end{aligned} \tag{8}$$

where $\varepsilon_{jTE}^{(2)}$ was the second-order approximation of the effective permittivity (jth layer of the tip) for the TE wave, β was the design constant which was defined as:

$$\beta = \frac{1}{(n_{PI} + n_{air})\frac{d_2}{\lambda}} \tag{9}$$

$\Delta\varepsilon_j$ was the second-order correction factor for the effective permittivity (jth layer of the tip) for the TE wave:

$$\Delta\varepsilon_j = \frac{\pi^2}{3}\varepsilon_0 f_j^2 (1 - f_j)^2 \frac{(n_{PI} - n_{air})^2}{\varepsilon_{jTE}^{(0)}} \tag{10}$$

It is necessary to replace the effective permittivity with the effective refractive index, as the reflectivity was a direct function of the refractive index rather than the permittivity. The zeroth-order approximation of the effective refractive index (jth layer of the tip) for the TE wave was represented by:

$$n_{jTE}^{(0)} = \sqrt{\frac{\varepsilon_{jTE}^{(0)}}{\varepsilon_0}} \tag{11}$$

where $n_{jTE}^{(0)}$ was the zeroth-order approximation of the effective refractive index (jth layer of the tip) for the TE wave.

When wavelength is only a few times larger than the structure, the second-order approximation of the effective refractive index (jth layer of the tip) was:

$$n_{jTE}^{(2)} = n_{jTE}^{(0)}(1 + \Delta n_j) \tag{12}$$

where $n_{jTE}^{(2)}$ was the second-order approximation of the effective refractive index (jth layer of the tip) for the TE wave, Δn_j was the second-order correction factor for the effective refractive index (jth layer of the tip) for the TE wave:

$$\Delta n_j = \sqrt{1 + \frac{\Delta\varepsilon_j}{\beta^2}} - 1 \tag{13}$$

$n_{jTE}^{(2)}$ was derived from the above equations.

$$n_{jTE}^{(2)} = \sqrt{f_j n_{PI}^2 + (1 - f_j) n_{air}^2 + \frac{\pi^2}{3}\left(\frac{d_2}{\lambda}\right)^2 f_j^2 (1 - f_j)^2 (n_{PI}^2 - n_{air}^2)^2} \tag{14}$$

where $n_{jTE}^{(2)}$ was the second-order approximation of the effective refractive index (jth layer of the tip) for the TE wave, f_j was the filling rate of jth layer of the tip, n_{PI} was the refractive index of the polyimide, n_{PI} = 1.55, and n_{air} was the refractive index of the air, n_{air} = 1, λ was the wavelength, and d_2 was the width of the cube.

Taking the incident light wavelength of 1100 nm as an example, the variable in the equation was the filling rate f_j. The curves of the effective refractive index of micro-nano structures with different tip heights as a function of thickness are shown in Figure 4.

As shown in Figure 4, the refractive index changes abruptly when the incident light is incident from air to the tip of the micro-nano structure, resulting in an increase in the reflectivity. The refractive index of the effective multilayer structure increased slowly when the incident light was incident on the tip with a height of 600 nm. As the height of the tip decreased, the gradient of the effective refractive index gradually increased. When the incident light was incident on the tip with a height of 50 nm, the effective refractive index changed abruptly, and the gradient of the curve was maximum. According to Fresnel's law, the reflectivity was maximum when height equals 50 nm. Therefore, at a wavelength of

1100 nm, the effective refractive index changed abruptly, and the reflectivity increased as the height of the tip of the micro-nano structure decreased.

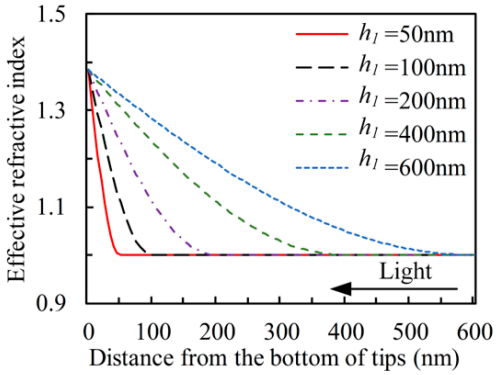
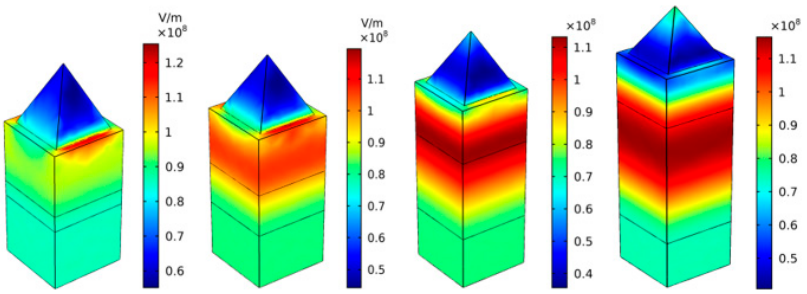
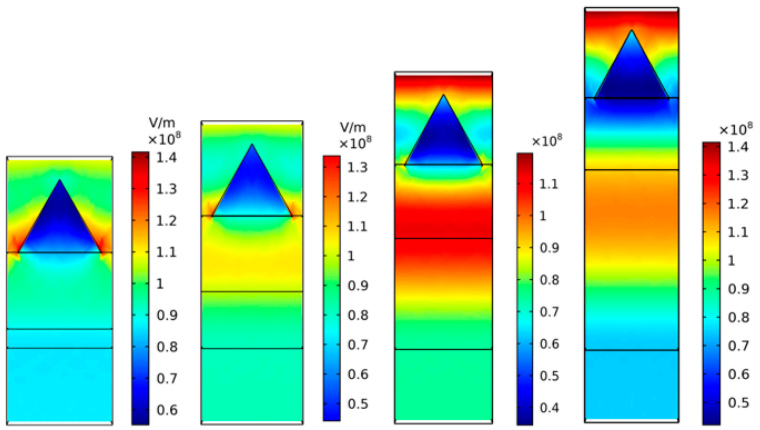


Figure 4. Effective refractive index of micro-nano structures with different heights of tips varied with the distance from the bottom of tips.

Figure 5a–d show images of three-dimensional and central cross-sectional distributions of the electrical field intensities for the pyramidal micro-nano structures with a variety of air gaps (50, 150, 300, and 500 nm) under the wavelength of 1.54 μm (a and b) and 5.99 μm (c and d), respectively. As the air gap was increased, the electric field intensity at the incident port was shown to increase at 1.54 μm, indicating that a higher portion of the incident light was reflected back. As to the electric field intensity at 5.99 μm, no significant changes were found.

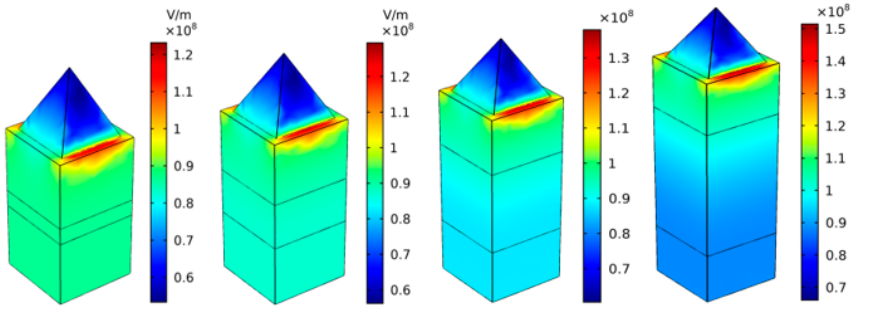


(**a**)

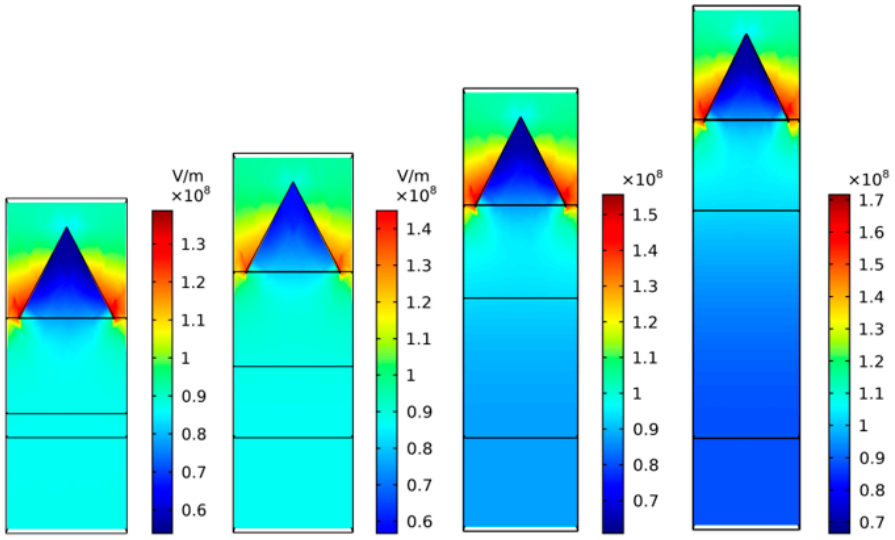


(**b**)

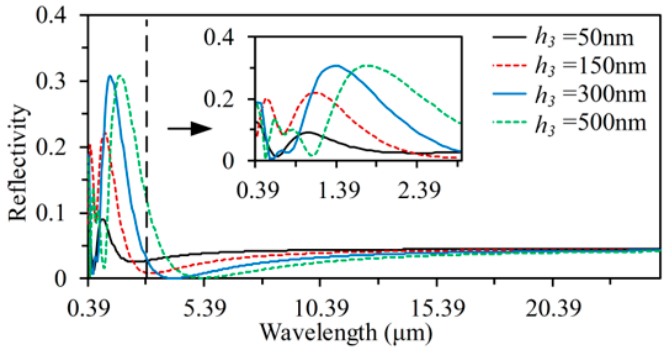
Figure 5. *Cont.*



(**c**)



(**d**)



(**e**)

Figure 5. Numerical results of spectral characteristics of pyramidal biomimetic micro-nano structures as a function of air gap. Images of three-dimensional and central cross-sectional distributions of the electrical field intensity for the pyramidal micro-nano structures with a variety of air gaps (50, 150, 300, and 500 nm) under the wavelength of 1.54 μm (**a**,**b**) and 5.99 μm (**c**,**d**), respectively. (**e**) Spectral reflectance curves of pyramidal biomimetic micro-nano structures modulated by air gap, indicating that an increase of air gap can decrease the solar absorptance and increase the infrared emissivity.

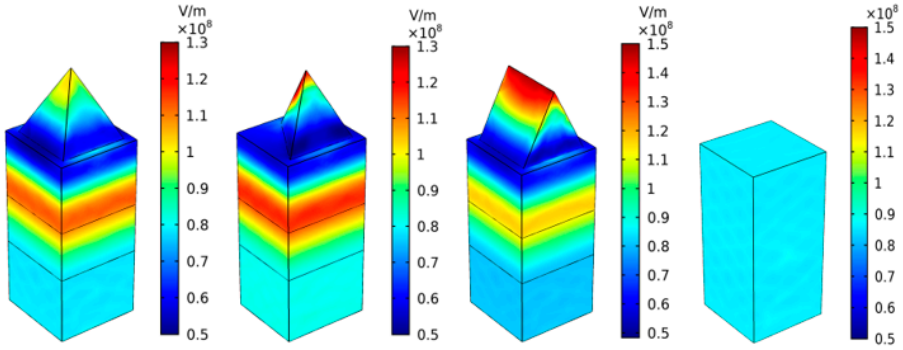
Figure 5e shows spectral reflectance curves of pyramidal biomimetic micro-nano structures modulated by the air gap. As the air gap was increased, the maximum reflectivity in visible and near-infrared ranges of the spectrum (0.39~2.5 μm) increased, while the reflectivity in the mid-infrared range of the spectrum (2.5~25 μm) was decreased, revealing that as the air gap was increased, the solar absorptance decreased, and the infrared emissivity increased. When the air gap was higher than 300 nm, with the further increase of the air gap, the peak reflectivity curve no longer increased with a phenomenon of red shift observed.

Inspired by the hairs of Saharan silver ants, Wu et al. [14] fabricated flexible hair-like photonic structures. The biomimetic flexible films were applied to the glass substrate to form two kinds of air gaps, which involved either a triangular air gap or a bridge-like air gap. It confirmed the role of the air gap in enhancing optical reflections and that different kinds of air gaps led to different reflection enhancement effects. This article further studied the thickness of the air gap, which was a supplement to the previous study.

It was speculated that the Mie scattering inside the micro/nano structure enhanced the reflectivity in the visible and near-infrared ranges of the spectrum, but the near-field coupling between the film and the body of the micro-nano structure reduced the intensity of Mie scattering, weakening the enhancement effect of the reflection by the Mie scattering. Therefore, at an air gap less than 300 nm, as the air gap was increased, the near-field coupling effect became weaker with increasing intensity of Mie scattering, and thus the reflectivity in the visible and near-infrared ranges of the spectrum increased.

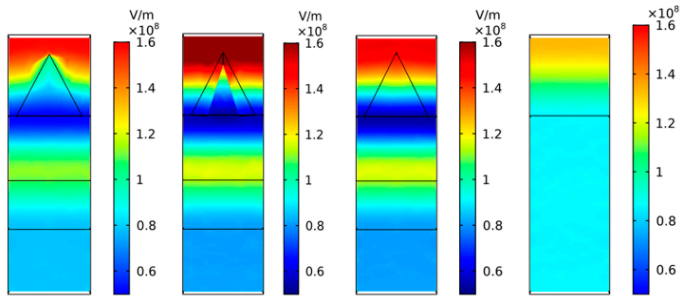
When the air gap increased above 300 nm, the near-field coupling effect between the film and the body of the micro-nano structure no longer changed, and the intensity of Mie scattering no longer increased; therefore, the peak of reflectivity no longer increased. As the air gap increased, the basic modes of Mie scattering moved toward larger wavelengths. Therefore, when the air gap increased from 300 nm to 500 nm, the peak value of the reflectivity curve did not change, but there was a red-shift phenomenon.

Figure 6a–d show images of three-dimensional and central cross-sectional distributions of the electrical field intensities for the biomimetic micro-nano structures based on four types of structures (pyramid (I), tetrahedron (II), triangular prism (III) and flat surface (IV)) under the wavelength of 0.99 μm (a and b) and 7.99 μm (c and d), respectively. The electric field intensities of the incident ports of three micro-nano structures at 0.99 μm were higher than the counterparts inside the structure, indicating that most of the incident light was reflected back. Meanwhile, the electric field intensity of the incident port of the flat polyimide film was not much different from the inside, indicating a low degree of light reflection.

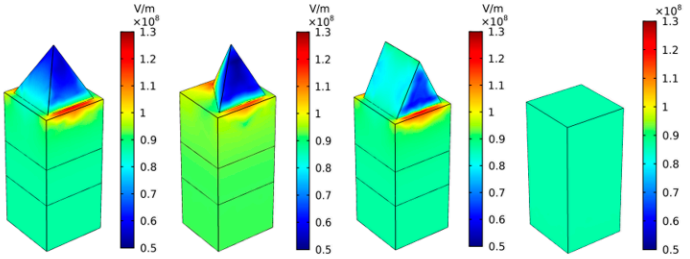


(**a**)

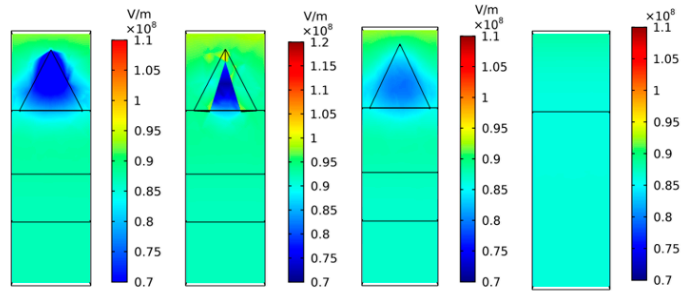
Figure 6. *Cont.*



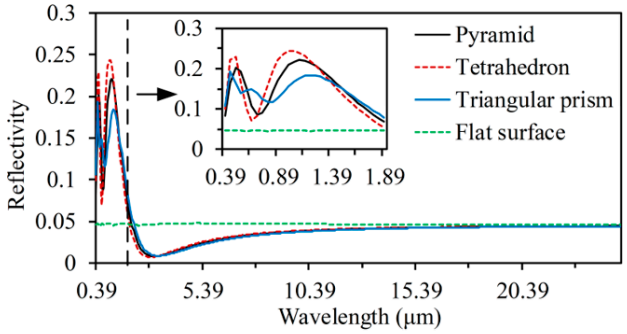
(**b**)



(**c**)



(**d**)



(**e**)

Figure 6. Numerical results of spectral characteristics of biomimetic micro-nano structures based on pyramid (I), tetrahedron (II), triangular prism (III) and flat surface (IV) with air gap for comparison. Images of three-dimensional and central cross-sectional distributions of the electrical field intensity for the biomimetic micro-nano structures based on these four types of structures under the wavelength of 0.99 μm (**a**,**b**) and 7.99 μm (**c**,**d**), respectively. (**e**) Spectral reflectance curves of biomimetic micro-nano structures modulated by these four types of structures indicate that biomimetic micro-nano structures can decrease the solar absorptance to block the incidence of heat flow from the sun and increase the infrared emissivity to dissipate its own heat to the space.

Figure 6e shows spectral reflectance curves of biomimetic micro-nano structures modulated by these four types of structures. The reflectivity of the pyramid, tetrahedron and triangular prism based micro-nano structures with an air gap in the visible and near-infrared ranges of the spectrum (0.39~2.5 μm) were greatly enhanced compared with the flat polyimide film. Among them, the reflectivity peak of the tetrahedral based micro-nano structure was maximum. In the mid-infrared range of the spectrum (2.5~25 μm), the reflectivity of three micro-nano structures was slightly lower than that of the flat surface. The three types of micro-nano structures demonstrated little differences in spectral characteristics, but compared with the flat polyimide film, they decreased the solar absorptance to block the incidence of heat flow from the sun and increased the infrared emissivity to dissipate heat to space.

4. Conclusions

In this paper, biomimetic micro-nano structures derived from Saharan silver ants were introduced into aerospace microwave-transmitting thermal control materials, the influences of tip heights, air gaps and structures on the spectral characteristics of which were studied by numerical simulation.

The following conclusions were drawn:

(1) Spectral characteristics of the biomimetic micro-nano structures were mainly controlled by the tip heights and the air gaps among the three influencing factors.
(2) The solar absorptance and the infrared emissivity were decreased with the decrease of the tip height.
(3) The solar absorptance was decreased, and the infrared emissivity was increased with the increase of the air gap within a certain scale. When the air gap was above a certain scale, there was a red-shift phenomenon of the reflectivity curve.
(4) The spectral characteristics of three types of structures (pyramid, tetrahedron and triangular prism) with air gap were similar and compared with the flat surface without air gap, the reflectivity in the solar spectrum was larger (the solar absorptance was lower), and the reflectivity in the infrared waveband was lower (the infrared emissivity was larger).

This study provided guidance for further engineering and applications of the biomimetic micro-nano structures derived from Saharan silver ants in spacecraft with microwave detection equipment. This structure extended ranges of structures and materials for thermal control surface units of spacecraft. It had potential benefits for microwave transmission, heat protection, heat dissipation and resistance to damage caused by radiation.

Supplementary Materials: The following supporting information can be downloaded at: https://www.mdpi.com/article/10.3390/coatings13010085/s1, Figure S1: Simulation structures of the hair of the sliver ant including two-dimensional (a) and three-dimensional (b) models, from top to bottom (I) air, (II) triangular hair, (III) air gap and (IV) body; Figure S2: Numerical results of spectral characteristics of the Saharan silver ant: images of central cross-sectional distributions of the electrical field intensity for the hair under the wavelength of 0.652 μm, 0.909 μm, 1.333 μm, 1.704 μm, and 2.880 μm, obtained by the simulation of Ref. [11] (a) and this study (b), where the distributions of the electric field intensities were comparable. Spectral reflectance curves of Saharan silver ants were obtained by Ref. [11] (c) and this study (d), where the peak positions of the two curves were consistent.

Author Contributions: Conceptualization, M.L. and B.C.; methodology, M.L.; investigation, M.L.; data curation, M.L.; writing—original draft preparation, M.L.; writing—review and editing, J.C.; funding acquisition, B.C. and D.Z. All authors have read and agreed to the published version of the manuscript.

Funding: This research was funded by the National Natural Science Foundation of China, grant number 61805253.

Institutional Review Board Statement: Not applicable.

Informed Consent Statement: Not applicable.

Data Availability Statement: The data that support the findings of this study are available from the corresponding author upon reasonable request.

Conflicts of Interest: The authors declare no conflict of interest.

References

1. Holynska, M.; Tighe, A.; Semprimoschnig, C. Coatings and Thin Films for Spacecraft Thermo-Optical and Related Functional Applications. *Adv. Mater. Interfaces* **2018**, *5*, 20. [CrossRef]
2. Qiu, X.L.; Zhou, Y.R.; Shen, Z.C. Electrical Property Degradation and Mechanism of Aerospace White Paint Irradiated by Space Near UV Irradiation. *Open Cybern. Syst. J.* **2015**, *9*, 138–141. [CrossRef]
3. Zeng, Y.B.; Xiong, C.X.; Liu, W.Y.; Feng, W.Q. The Effects of UV, Electrons and Protons on Selection of Binders and Pigments for White Thermal Control Coatings. In Proceedings of the 9th International Symposium on Materials in a Space Environment, Noordwijk, The Netherlands, 16 June 2003.
4. Rogers, J.E.; Warniak, J.S.; Hobrock, L.M.; Bafico, M.A.; Scheele, S.R. Thermal Protective Shield for Antenna Reflectors. U.S. Patent No. 4,479,131, 23 October 1984.
5. Lepore, A.; Wong, H.; Marr, S.L.; Amore, L.J. RF-Transparent Antenna Sunshield Membrane. European Patent No. EP93911344B1, 18 May 1993.
6. Esther, A.C.M.; Sridhara, N.; Sebastian, S.V.; Bera, P.; Anandan, C.; Rangappa, D.; Sharma, A.K.; Dey, A. Evaluation of Nanoalumina Coated Germanium Black Polyimide Membrane as Sunshield for Application on the Communication Satellite Antenna. *Ceram. Int.* **2016**, *42*, 2589–2598. [CrossRef]
7. Esther, A.C.M.; Dey, A.; Sridhara, N.; Yougandar, B.; Bera, P.; Anandan, C.; Rangappa, D.; Sharma, A.K. A Study on Degradation of Germanium Coating on Kapton Used for Spacecraft Sunshield Application. *Surf. Interface Anal.* **2015**, *47*, 1155–1160. [CrossRef]
8. Lipovsek, B.; Krc, J.; Isabella, O.; Zeman, M.; Topic, M. Modeling and Optimization of White Paint Back Reflectors for Thin-Film Silicon Solar Cells. *J. Appl. Phys.* **2010**, *108*, 103115. [CrossRef]
9. Metwally, S.; Comesana, S.M.; Zarzyka, M.; Szewczyk, P.K.; Karbowniczek, J.E.; Stachewicz, U. Thermal Insulation Design Bioinspired by Microstructure Study of Penguin Feather and Polar Bear Hair. *Acta Biomater.* **2019**, *91*, 270–283. [CrossRef]
10. Cui, Y.; Gong, H.X.; Wang, Y.J.; Li, D.W.; Bai, H. A Thermally Insulating Textile Inspired by Polar Bear Hair. *Adv. Mater.* **2018**, *30*, 8. [CrossRef] [PubMed]
11. Shi, N.N.; Tsai, C.C.; Camino, F.; Bernard, G.D.; Yu, N.F.; Wehner, R. Keeping Cool: Enhanced Optical Reflection and Radiative Heat Dissipation in Saharan Silver Ants. *Science* **2015**, *349*, 298–301. [CrossRef] [PubMed]
12. Wehner, R.; Marsh, A.C.; Wehner, S. Desert Ants on A Thermal Tightrope. *Nature* **1992**, *357*, 586–587. [CrossRef]
13. Zhai, Y.; Ma, Y.G.; David, S.N.; Zhao, D.L.; Lou, R.N.; Tan, G.; Yang, R.G.; Yin, X.B. Scalable-Manufactured Randomized Glass-Polymer Hybrid Metamaterial for Daytime Radiative Cooling. *Science* **2017**, *355*, 4. [CrossRef] [PubMed]
14. Wu, W.C.; Lin, S.H.; Wei, M.M.; Huang, J.H.; Xu, H.; Lu, Y.H.; Song, W.J. Flexible Passive Radiative Cooling Inspired by Saharan Silver Ants. *Sol. Energy Mater. Sol. Cells* **2020**, *210*, 9. [CrossRef]
15. Beckers, M.; Weise, B.; Kalapis, S.; Gries, T.; Seide, G.; Bunge, C.A. Basics of light guidance. In *Polymer Optical Fibres*; Bunge, C.A., Gries, T., Beckers, M., Eds.; Woodhead Publishing, Ltd.: Cambridge, UK, 2017; pp. 9–46.
16. Tian, Y.; Liu, X.; Chen, F.; Zheng, Y. Perfect grating-Mie-metamaterial based spectrally selective solar absorbers. *OSA Contin.* **2019**, *2*, 3223–3239. [CrossRef]
17. Raguin, D.H.; Morris, G.M. Antireflection Structured Surfaces for the Infrared Spectral Region. *Appl. Opt.* **1993**, *32*, 1154–1167. [CrossRef] [PubMed]

Disclaimer/Publisher's Note: The statements, opinions and data contained in all publications are solely those of the individual author(s) and contributor(s) and not of MDPI and/or the editor(s). MDPI and/or the editor(s) disclaim responsibility for any injury to people or property resulting from any ideas, methods, instructions or products referred to in the content.